GEOPHYSICS

Seismic evidence for global basalt accumulation in the mantle transition zone

Chunquan Yu[1,2]*, Saskia Goes[3], Elizabeth A. Day[3], Robert D. van der Hilst[4]

The mantle's compositional structure reflects the thermochemical evolution of Earth. Yet, even the radial average composition of the mantle remains debated. Here, we analyze a global dataset of shear and compressional waves reflecting off the 410- and 660-km discontinuities that is 10 times larger than any previous studies. Our array analysis retrieves globally averaged amplitude-distance trends in SS and PP precursor reflectivity from which we infer relative wavespeed and density contrasts and associated mantle composition. Our results are best matched by a basalt-enriched mantle transition zone, with higher basalt fractions near 660 (~40%) than 410 (~18–31%). These are consistent with mantle-convection/plate-recycling simulations, which predict that basaltic crust accumulates in the mantle transition zone, with basalt fractions peaking near the 660. Basalt segregation in the mantle transition zone also implies that the overall mantle is more silica enriched than the often-assumed pyrolitic mantle reference composition.

INTRODUCTION

While it is well established that Earth's mantle is a dominantly thermally driven convective system, compositional heterogeneity (including volatiles) is important for chemical cycling through Earth's interior. In the early 1960s, Ringwood (*1*) proposed the concept of pyrolite (containing ~60% olivine, Mg_2SiO_4 with some iron (Fe)] as a hypothetical model for the bulk chemistry of the upper mantle based on melting relationships and samples from the shallow mantle and surface. Subsequent petrological and geochemical studies argued that pyrolite could well be representative of the average composition of the whole mantle (*2*–*4*). However, systematic differences between pyrolite and bulk silicate Earth estimates based on CI chondrites left open the possibility that the mantle is—on average—more silica-rich than pyrolite (*2*, *3*, *5*, *6*). It has long been debated whether any radial compositional layering is maintained within the mantle, canonically, in the upper and lower mantle, and if and how this would affect the scale of mantle convection (*7*–*11*).

Plate tectonics continuously introduces into Earth's mantle the components of subducted plates, that is, a magmatic (basaltic) crust and a depleted (harzburgitic) residue (*12*, *13*). Because the entire volume of the mantle has been processed through mid-ocean ridges (that is, differentiated into melt and residue) at least once over the age of Earth (*13*) and the rate of chemical diffusion is too slow to homogenize mantle rocks (*14*), a mechanical mixture of basaltic and harzburgitic components likely makes up the bulk of the mantle. In addition, there may be a small amount of compositionally distinct material remaining from early Earth history (*15*, *16*). Even in a convective system involving the whole mantle, this can result in variations in composition with depth (*11*, *17*, *18*).

To test what composition best describes mantle compositional heterogeneity, it is typically parameterized as the above-mentioned mechanical mixture of basaltic and harzburgitic components and their respective phase equilibria, defined by the proportion and composition of mineral phases in (thermo)dynamic equilibrium [e.g., (*19*)]. Hereinafter, the mechanical mixture and equilibrium assemblage models are referred to as MM and EA, respectively, and their pyrolitic endmembers as PMM and PEA. Mapping the distribution of compositional heterogeneity is challenging, because in much of the mantle, seismic waves, our best deep Earth probes, are most sensitive to variations in temperature.

The mantle transition zone (MTZ), bounded by two major seismic discontinuities at about 410 and 660 km in depth (hereafter referred to as 410 and 660), is a zone of relatively large wavespeed-depth gradients. There is a general agreement (*6*, *20*, *21*) that 410 is associated with an exothermic phase change from olivine to wadsleyite, which enhances flow, and 660 with an endothermic phase change from the olivine-polymorph ringwoodite to bridgmanite and ferropericlase, which tends to hamper flow between upper and lower mantle (*22*–*24*). In thermochemical convection models that include differentiated plates, differences in the pressure-temperature conditions of solid-state phase transitions in basaltic and harzburgitic compositions can cause radial variations in the concentrations of the two components across the MTZ (*11*, *17*, *18*, *25*). Thus, the MTZ regulates mass and heat transfer between the upper and lower mantle, making it a key region to study the thermochemical structure of the mantle.

The topography of 410 and 660 or, rather, MTZ thickness (the distance between 410 and 660) has been widely used to infer MTZ temperature (*26*–*33*) because it has limited sensitivity to mantle composition (*34*). On the other hand, mantle composition strongly affects the wavespeed and density (or impedance) contrasts across 410 and 660. Experimental data and thermodynamic modeling show that impedance contrasts across 410 and 660 are to a large extent controlled by the olivine fraction (or, conversely, basalt fraction in MM) of mantle composition, with a higher olivine fraction (or lower basalt fraction) resulting in larger impedance contrasts (*34*–*36*).

[1]Department of Earth and Space Sciences, Southern University of Science and Technology, Shenzhen 518055, China. [2]Guangdong Provincial Key Laboratory of Geophysical High-resolution Imaging Technology, Southern University of Science and Technology, Shenzhen 518055, China. [3]Department of Earth Science and Engineering, Imperial College London, London SW7 2BP, UK. [4]Department of Earth, Atmospheric and Planetary Sciences, Massachusetts Institute of Technology, Cambridge, MA 02139, USA.
*Corresponding author. Email: yucq@sustech.edu.cn

Wavespeed and density contrasts across 410 and 660 can be inferred from the amplitudes of seismic waves reflected or converted at these boundaries. Precursors to the surface reflected phases SS and PP, reflecting off mantle discontinuities roughly midway between earthquake sources and receivers (Fig. 1A), give better global coverage than methods such as receiver functions, triplicated waveforms, ScS reverberations, or P′P′ precursors [e.g., (*32*)]. Previous studies estimated wavespeed and density (or impedance) contrasts across 410 and 660 using either stacked amplitudes or amplitude versus offset (AVO) analyses of SS and PP precursors (*33*, *37*–*43*). Growth of the global dataset of seismic waveforms allows us to analyze an order of magnitude more data than previous studies. Furthermore, with novel array processing techniques to filter out interfering phases and suppress random noise (*44*), we can expand the AVO analysis of the weak 410 and 660 precursors over a substantially larger range of offsets (Fig. 2), which allows for more robust contrast estimation. We focus here on the globally averaged characteristics of 410 and 660 and, thus, on average MTZ temperature and composition.

RESULTS

AVO trends

Figure 2 (A and B) shows our global stack of SS and PP waveforms as a function of epicentral distance. Results are averaged over 768 evenly distributed (reflection point) caps of 10° radius (Fig. 1, C and D) to suppress noise and minimize the bias of the uneven data distribution on the global stacks. For the SS and PP stacks, respectively, a total number of ~0.95 and ~1.21 million seismograms, bandpass-filtered between 20 and 50 s, from ~3500 $M \geq 6.0$ shallow-focus (0 to 70 km) earthquakes, which occurred between 2000 and 2017, were selected (Materials and Methods). Interfering phases and random noise are removed using the curvelet-based array denoising algorithm developed by Yu *et al.* (*44*) (and further verified using synthetic waveform modeling; figs. S1 and S2). This allows us to observe SS and PP precursors from both 410 and 660 continuously over a wide distance range from 70° to 170° (Fig. 2, C and D, and fig. S3). The results are robust with respect to the choice of data quality criteria (figs. S4 and S5).

We measure amplitude ratios of SS and PP precursors relative to their reference phases (that is, A_{S410S}/A_{SS}, A_{S660S}/A_{SS}, A_{P410P}/A_{PP}, and A_{P660P}/A_{PP}) as a function of epicentral distance. Following Yu *et al.* (*45*), we recover reflection coefficient ratios of SS and PP precursors relative to their reference phases (that is, R_{S410S}/R_{SS}, R_{S660S}/R_{SS}, R_{P410P}/R_{PP}, and R_{P660P}/R_{PP}) by estimating and removing effects of geometrical spreading and intrinsic attenuation and incoherent stacking using global variations in their arrival times (Materials and Methods; figs. S6 to S8). The thus corrected reflection coefficient ratios (Fig. 3 and fig. S9) are not very different from the original amplitude ratios due to the similarity of the propagation paths of the surface and discontinuity reflected phases, and the fact that possible effects are opposite in sign so that they largely cancel each other out. There are some undulations in amplitude versus distance, which may reflect measurement uncertainty, regional variation combined with uneven sampling, and/or imperfect removal of interfering phases and noise (Fig. 3 and fig. S2). SS and PP stacks using only deep-focus (>70 km) earthquakes, which to our knowledge have not been used before, yield similar results but with a slightly higher noise level, mainly due to fewer (~0.31 and ~0.38 million traces for SS and PP stacks, respectively) and less even data sampling (figs. S10 and S11).

We identify S410S and P410P and S660S over a wider range of distances than previously possible, which provides stronger constraints on the shape of the reflectivity curves, including a clear minimum in reflection for S660S (Fig. 3). The retrieved AVO trends are similar (Fig. 3) to those expected from forward

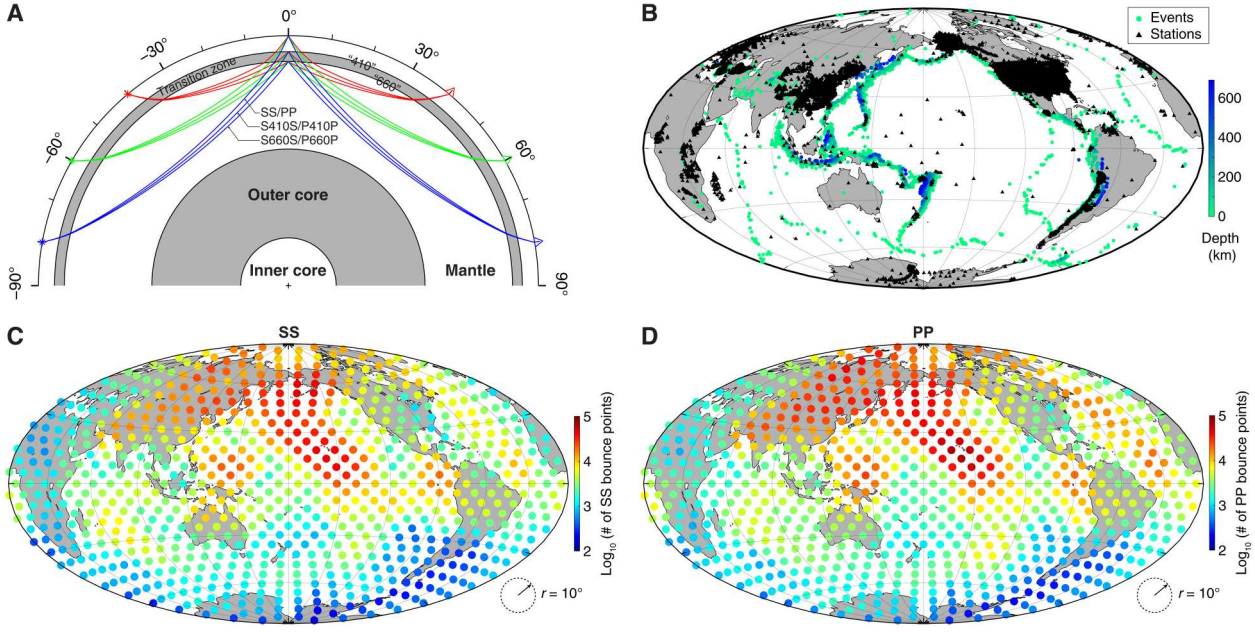

Fig. 1. SS and PP precursors. (**A**) Ray paths of SS (or PP) and their precursors from 410 and 660. (**B**) Global distribution of events and stations used in this study. (**C** and **D**) Density of SS and PP bounce points, respectively. We use (768) evenly distributed caps of 10° radius to reduce effects of the uneven distribution of sampling points.

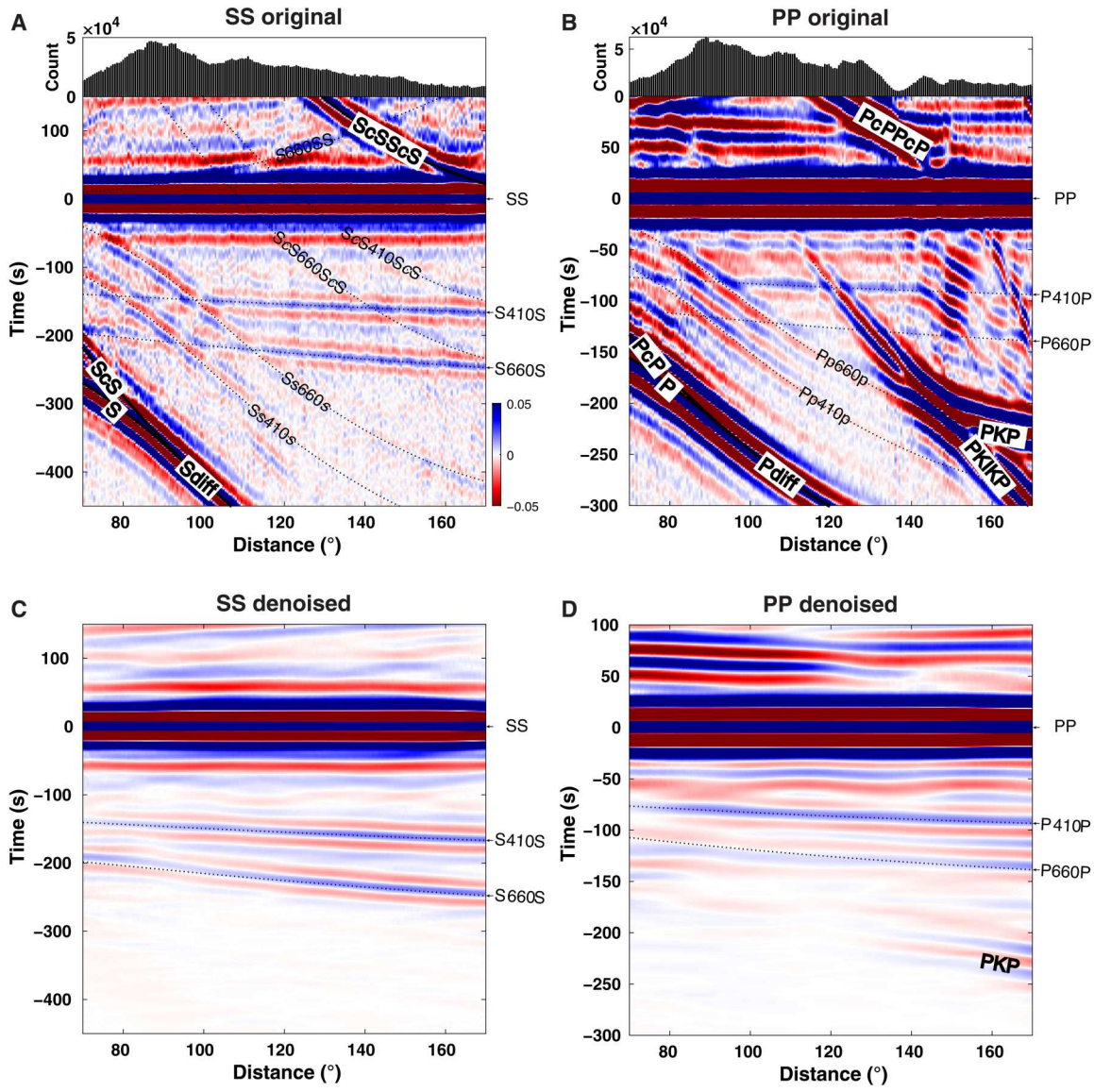

Fig. 2. Global stacks of SS and PP waveforms. (**A** and **B**) Original SS and PP stacks, respectively, averaged over all caps to derive best-estimate global stacks. Only events with focal depth less than 70 km are used in these stacks. (**C** and **D**) Denoised SS and PP stacks, respectively. Thin dotted lines mark predicted phase arrivals based on ray theory. Note that SS and PP precursors from 410 and 660 are clearly and continuously observed in the denoised stacks. Residuals are shown in fig. S3.

calculations of global seismic reference models Preliminary Reference Earth Model (PREM) (*46*) and ak135 (*47*, *48*) as well as thermodynamic models for a range of plausible mantle compositions (Materials and Methods and discussed below). However, reflectivity is lower than predicted by PREM and ak135 for all phases except P410P. In contrast to previous studies (*33*, *37*, *38*, *42*), P660P is visible, albeit weak, over most of the distance range (Figs. 2D and 3D).

Wavespeed and density contrasts across 410 and 660

Reflection coefficients of SS and PP precursors (R_{S410S}, R_{S660S}, R_{P410P}, and R_{P660P}) are mainly affected by wavespeed and density contrasts across 410 and 660 (except when reflection coefficients are close to zero, which will be investigated below). Following Shearer and Flanagan (*38*), hereinafter SF1999, we assume that the recovered reflection coefficient ratios are representative of the globally averaged one-dimensional (1D) structural properties of the Earth and apply a grid search to find the best fitting *P*-wavespeed, *S*-wavespeed, and density contrasts ($\Delta\alpha$, $\Delta\beta$, and $\Delta\rho$) across 410 and 660. This reveals how well the contrasts are constrained and allows comparison with earlier work and with thermodynamic constraints on the relation between wavespeeds and density. We calculate synthetic reflection coefficients of SS and PP precursors using Zoeppritz equations (*49*), where mean wavespeeds and density at 410 and 660 are taken from those of ak135 by averaging the values directly above and below the discontinuities. The near-surface reflection coefficients (R_{SS} and R_{PP}) are calculated using a half-space crustal model, although interference with Moho reflections and/or water reverberations can introduce uncertainty (Materials and Methods and figs. S12). We calculate the root

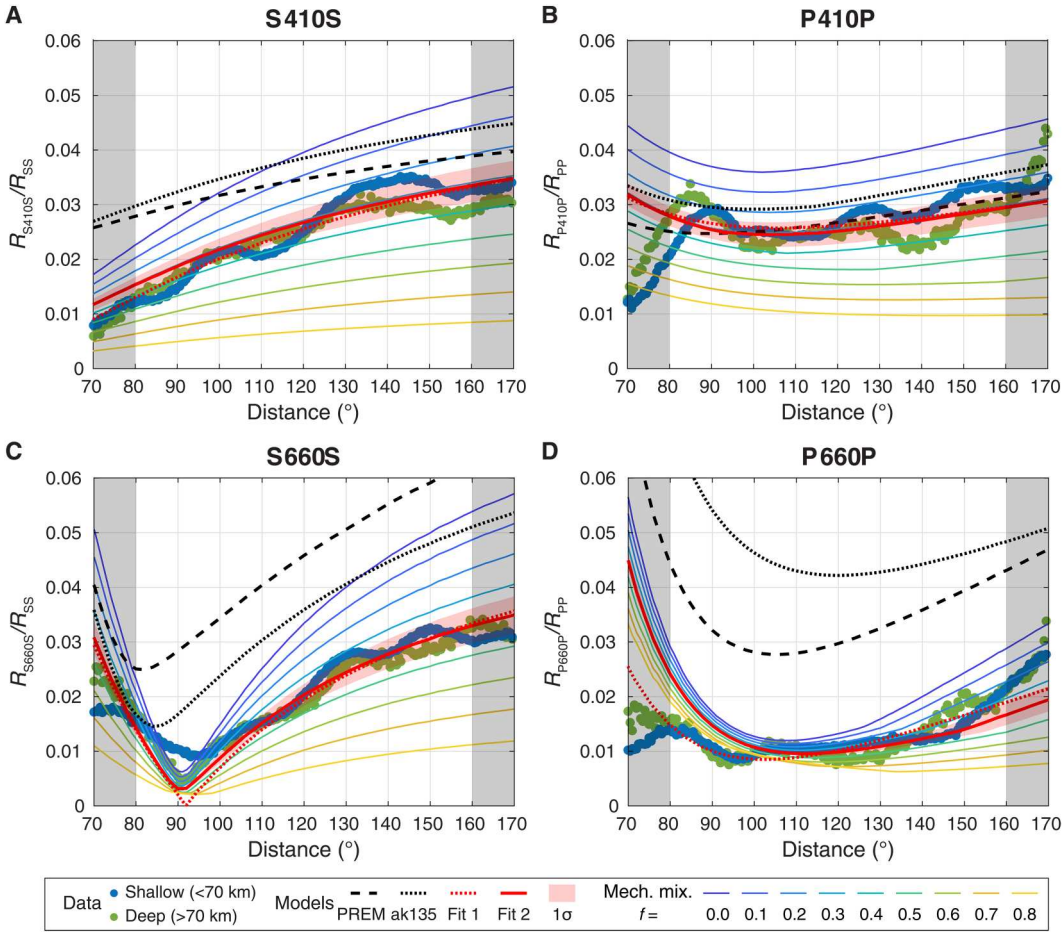

Fig. 3. Amplitude-versus-offset analysis of SS and PP precursors. (**A**) S410S, (**B**) P410P, (**C**) S660S, and (**D**) P660P. In each panel, blue and green circles are reflectivity of precursors (normalized by their reference phases; Materials and Methods) measured from global stacks of shallow- (<70 km; Fig. 2, C and D) and deep- (>70 km; fig. S10, B and E) focus events, respectively. Uncertainties estimated from bootstrap analysis are generally small (figs. S9 and S11) and not shown here. Synthetic reflectivity of precursors (normalized by their reference phases) are shown for the Preliminary Reference Earth Model (PREM) and ak135 reference Earth models, and mechanical mixture (MM) models with basalt fraction (*f*) ranging from 0 to 80% at T_{pot} = 1350°C using the stx11 database. We adjust absolute wavespeeds and density from thermodynamic models so that their mean values at 410 and 660 are close to those of ak135 (see Discussion). Dashed and solid red curves are best fitting reflectivity assuming a first-order sharp discontinuity (fit 1; by searching $\Delta\alpha$, $\Delta\beta$, and $\Delta\rho$ across the discontinuity) and a MM model (fit 2; by searching basalt fraction in MM), respectively. Reddish areas show the 1σ confidence interval of fit 2. Amplitude measurements in gray shaded areas are discarded to avoid edge effects of the denoising algorithm.

mean square error (RMSE) between synthetic and observed reflection coefficient ratios for 410 and 660, respectively. Figure 4 shows the distribution of averaged misfits for all epicentral distances between 80° and 160°, where amplitude measurements are most reliable. Our large dataset provides strong constraints on wavespeed and density contrasts across 410 and 660.

We find wavespeed contrasts at 410 ($\Delta\alpha_{410}$ = 5.2%, $\Delta\beta_{410}$ = 6.2%) that are higher than the widely used global seismic reference models PREM and ak135, not as high as the earlier precursor estimates by SF1999, and similar to those of the precursor and receiver function studies by Lawrence and Shearer (*41*) (LS2006; Fig. 4A). Our estimate of the density contrast ($\Delta\rho_{410}$ = 2.4%), which is well constrained due to the larger distance range of observations, is significantly lower than PREM and ak135 and estimates by LS2006 but higher than the estimate by SF1999. The $\Delta\rho_{410}$ estimates fall close to the trend between density and wavespeed contrasts expected from mineral physics, which includes a wide range of plausible mantle compositions (Fig. 4A).

For 660, the wavespeed and density contrasts in PREM and ak135 are significantly larger than inferred from earlier studies of reflected and converted waves (SF1999 and LS2006; Fig. 4B). We obtain similar density and *S*-wavespeed contrasts ($\Delta\rho_{660}$ = 4.2%, $\Delta\beta_{660}$ = 5.2%) as previous precursor and receiver function studies but require a higher *P*-wavespeed contrast ($\Delta\alpha_{660}$ = 3.2%). Our estimates of the ratios of wavespeed and density contrasts ($\Delta\alpha_{660}$:$\Delta\beta_{660}$:$\Delta\rho_{660}$) are consistent with those expected from mineral physics for a range of plausible mantle compositions (Fig. 4B).

Apparent moveouts of S660S and P660P

The apparent arrival time-versus-offset variations of SS and PP precursors also contain important information about elastic properties around the MTZ discontinuities. We pick apparent arrival times of SS and PP precursors at their maximum peaks. Note that due to

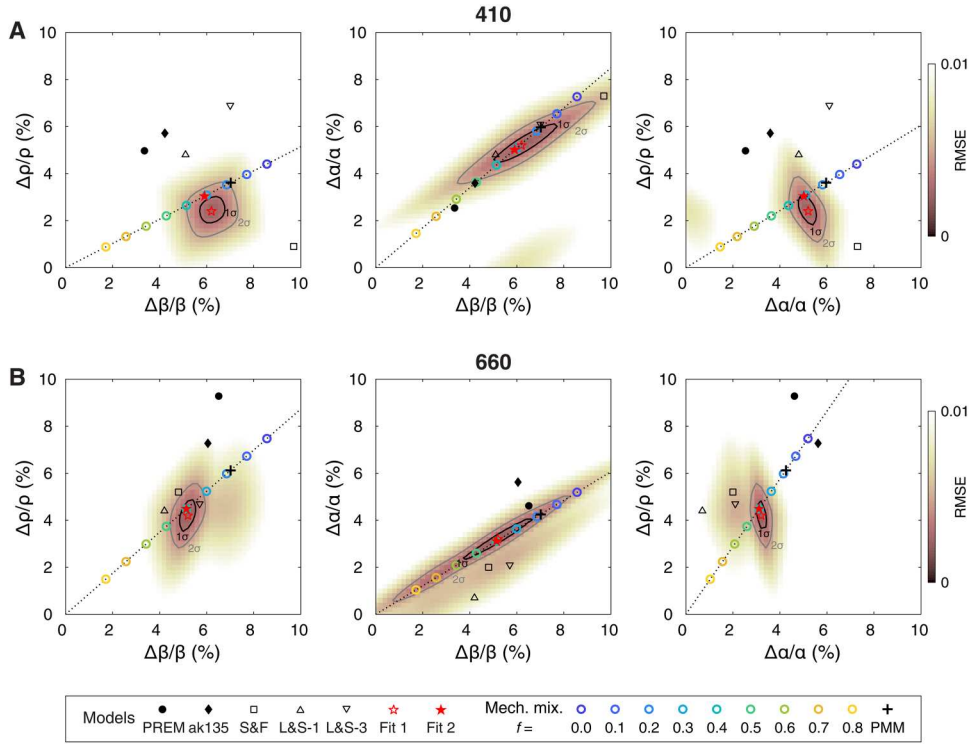

Fig. 4. Wavespeed and density contrasts across 410 and 660. (**A**) 410 and (**B**) 660. In each panel, the background shows the distribution of the root mean square error (RMSE) between observed and synthetic reflectivity of SS and PP precursors (Fig. 3). A first-order sharp discontinuity is assumed so that reflectivity is calculated by searching for $\Delta\alpha$, $\Delta\beta$, and $\Delta\rho$ across both discontinuities. The open red star shows the best fit (fit 1). Dark and gray contours mark 1σ and 2σ confidence intervals, respectively. Open circles are wavespeed and density contrasts measured from various mechanical mixture (MM) models at T_{pot} = 1350°C using the stx11 database, color coded by basalt fraction. The solid red star (fit 2) is measured from the best-fit MM model. Wavespeed and density contrasts from Preliminary Reference Earth Model (PREM) and ak135 and earlier estimates of Shearer and Flanagan (SF1999; S&F) and Lawrence and Shearer (LS2006; L&S-1 and L&S-3 are their best fit model parameters assuming sharp and gradual interfaces, respectively) are shown.

waveform distortions or polarity reversal related to complex structures or reflection coefficients, apparent arrival times can be different from ray-theoretical arrival times. For 410, apparent arrival times of S410S and P410P are in good agreement with ray-theoretical predictions (Fig. 5, A and B). However, apparent arrival times of S660S and P660P are more complicated. Both of them show an apparent moveout compared with ray-theoretical predictions (Fig. 5, A and B). The apparent moveout of S660S was previously observed beneath the central Pacific and was explained as a result of polarity change in R_{S660S} (*45*). The apparent moveout of P660P, however, cannot be explained by a first-order discontinuity at 660 (or a transitional interface) and is not consistent with predictions from thermodynamic models.

To understand what is needed to explain the apparent moveouts of S660S and P660P, we conduct a systematic survey of wavespeed and density contrasts around 660 (Materials and Methods). We perform 1D synthetic waveform modeling based on a propagator matrix algorithm, which computes the full reflectivity of SS and PP precursors free from contamination by interfering phases (*50*). The apparent moveout of S660S is associated with a minimum in the $|R_{S660S}|$ (Fig. 3C), which is most sensitive to $\Delta\rho_{660}/\Delta\beta_{660}$ and mean β_{660} (fig. S13). Using a mean β_{660} from ak135, we find a $\Delta\rho_{660}/\Delta\beta_{660}$ close to that predicted from thermodynamic models, which is about 0.87 (figs. S13). Synthetic waveform modeling confirms this result (figs. S14 and S15). For P660P, two conditions must be satisfied to explain the observed moveout. First, $\Delta\alpha_{660}/\Delta\beta_{660}$ must be ~0.54, which is smaller than predicted from the thermodynamic modeling (~0.61) but tightly constrained because the shape of the apparent moveout curve of P660P is very sensitive to $\Delta\alpha_{660}/\Delta\beta_{660}$ (figs. S16 and S17). These estimates could be used to constrain thermodynamic parameters. Second, the wavespeed and density gradient below 660 must not be smaller than that above 660; otherwise, an opposite moveout trend is expected (figs. S18 and S19). A model (fit 3) simplified from thermodynamic models that explains both the reflectivity and apparent moveout of SS and PP precursors is shown in Fig. 5C and table S1. These inferences from precursor amplitudes can help to refine the MTZ structure (discontinuity depths and wavespeed and density contrasts) in 1D global reference models obtained from fits to other types of seismic data.

DISCUSSION

Detectability of P660P

Detection of the P660P phase has been a challenge. Some studies attributed nondetection to continuity of Lamé's constant λ across 660 (*37*). Others attributed the observation of single or double reflections over a range of depths or detections only in some areas and not in others to a complicated nature of 660 attributed to variations in temperature or Al content (*33*, *40*). Waszek *et al.* (*33*) argued that

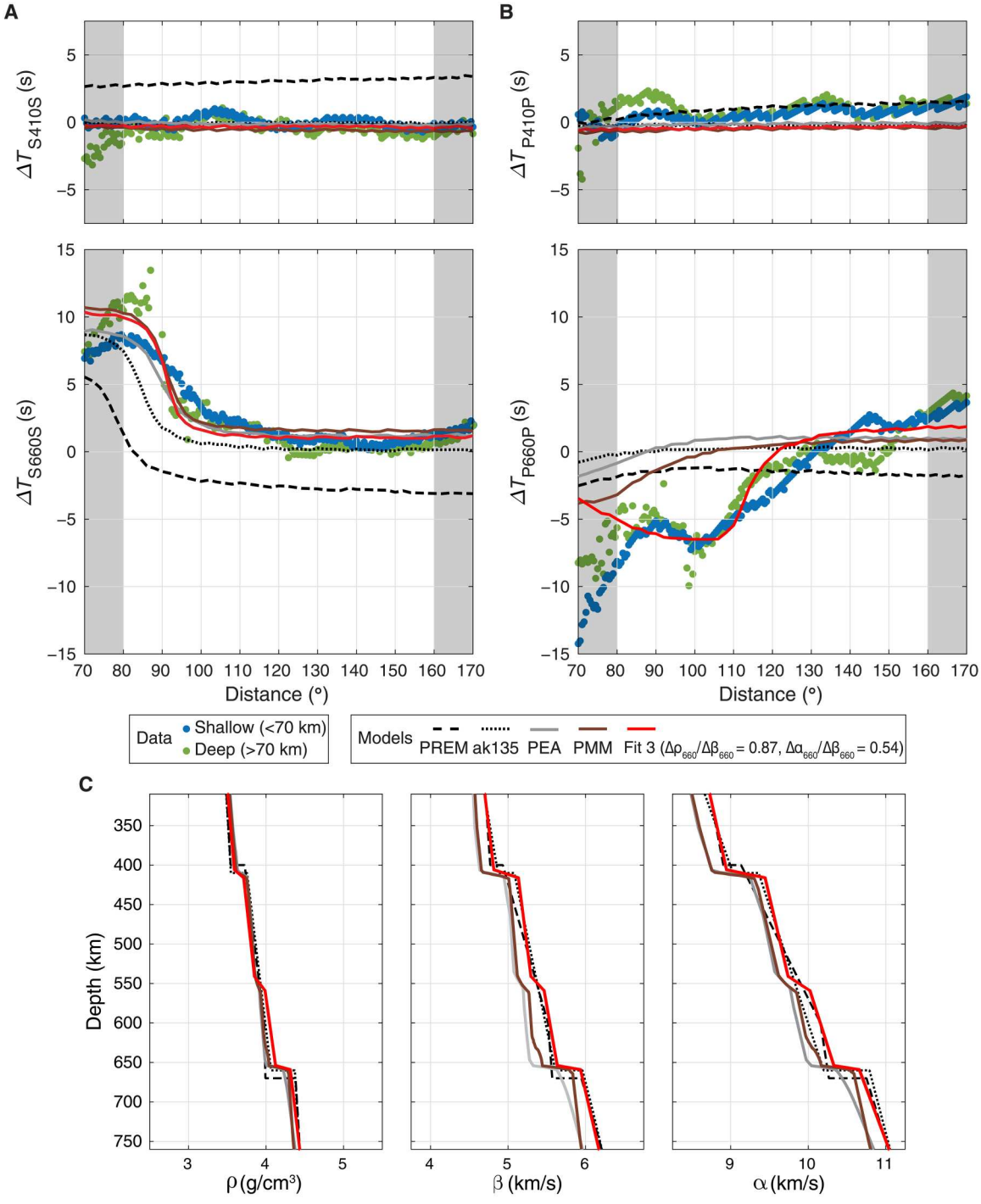

Fig. 5. Observed and synthetic apparent moveout of SS and PP precursors from 410 and 660. (**A**) SS and (**B**) PP precursors. In each panel, blue and green circles are observed apparent arrival times of precursors (by their maximum peaks) from global stacks of shallow- and deep-focus events, respectively. Apparent arrival time measurements in gray shaded areas are discarded to avoid edge effects of the denoising algorithm. Apparent arrival times of precursors measured from synthetic waveforms calculated from Preliminary Reference Earth Model (PREM), ak135, and thermodynamic models assuming PEA and PMM at T_{pot} = 1350°C using the stx11 database are shown. Apparent arrival times are reduced by ray theory calculations for the ak135 model. Red curves show the apparent moveout calculated from our preferred model (fit 3). (**C**) Wavespeed and density profiles across the mantle transition zone (MTZ). Red curves are our preferred model. Note that in synthetic waveform modeling, we slightly adjust the wavespeed and density profiles from thermodynamic models so that their mean values at 410 and 660 are close to those of ak135.

a mechanical mixture (PMM or basalt enriched MM) can explain the low visibility of P660P precursors. They reported P660P in the central Pacific, where temperature is expected to be high, but their apparent depth of 660 from P660P is larger than that from S660S. We show that, after array analysis, P660P can be observed in the global stack (albeit weak) over a wide distance range, whereas the signal was concealed by phase interference in the original stack (Fig. 2B). The low reflectivity of P660P may explain ubiquitous non-detection. The apparent moveout of P660P may explain previous reports of P660P over a wide depth range and will also decrease the effectiveness of slant-stack approaches. Our estimated $\Delta\alpha_{660}/\Delta\beta_{660}$ (~0.54) is higher than estimates (~0.4) by Estabrook and Kind (*37*), suggesting that, globally, Lamé's constant λ is not continuous across 660.

MTZ temperature

Previous studies inferred mantle potential temperature (T_{pot}) from MTZ differential travel times ($\Delta T_{S410S\text{-}S660S}$) or MTZ thickness. Ritsema *et al.* (*51*) used a self-consistent thermodynamic database stx08 (*34*) and found that differential travel times matched predictions from PMM at a T_{pot} consistent with shallow mantle petrological estimates (*52*–*54*) and that PEA required an unrealistically high T_{pot}. Waszek *et al.* (*33*) and Tauzin *et al.* (*43*) first converted their differential travel time observations to depth using a 3D global seismic velocity model (S40RTS) and subsequently found that their estimates of MTZ thickness were consistent with the thicknesses predicted using the updated database, stx11 (*19*), for shallow mantle T_{pot} estimates and a PMM composition.

We perform a similar set of thermodynamic calculations (Materials and Methods). Figure 6A illustrates that with stx08 the average global estimate of MTZ differential travel time from our study can be explained by PMM and a similar T_{pot} (~1350°C) as found by Ritsema *et al.* (*51*). With stx11, however, we cannot match the differential travel time with PMM or PEA. Within these two end-members, there is not a strong dependence on basalt fraction (Fig. 6A). The stx11 compilation predicts a lower dependence of MTZ differential travel time on T_{pot} than some previous studies (*34*, *55*). The trade-off between the change in MTZ thickness (decreasing by about ~12 km per 100°C increase in T_{pot}) and the average wavespeed in MTZ (with *S*-wavespeed decreasing by ~0.09 km/s ≈ 1.8% per 100°C increase in T_{pot}) results in a net effect of ~1.8-s decrease in differential travel time per 100°C increase in T_{pot}. The dependence of wavespeed estimates on thermodynamic data (*19*, *55*, *56*) makes it difficult to infer temperature from MTZ differential travel times (Fig. 6A).

For the next steps of our discussion we, therefore, fix T_{pot} based on shallow mantle petrological constraints (*52*–*54*), which is expected to be representative of internal mantle temperatures, and adjust all absolute wavespeeds accordingly. For stx11, we need to systematically increase *S*-wavespeed by ~3% at T_{pot} = 1300° to 1360°C (Fig. 6A). A similar shift in absolute *S*-wavespeed (somewhat dependent on basalt fraction) reconciles the same T_{pot} with the observed distance of the minimum in $|R_{S660S}|$ (Figs. 3C and 6B and fig. S13). Combined, these two constraints show that the MTZ-sensitive seismic data provide quite tight constraints on absolute *S*-wavespeed and require it to be close to that of ak135 (fig. S20). Note that Waszek *et al.* (*33*) and Tauzin *et al.* (*43*) in essence did a similar correction by using a seismic model (with absolute wavespeeds determined by the seismic 1D reference profile) to convert their travel times to depth before comparing with the thermodynamic models. For stx08, we cannot simultaneously match MTZ differential travel times and the distance of the minimum in $|R_{S660S}|$ (Fig. 6). A high concentration of volatiles in the MTZ, as some studies suggest (*57*), increases the discrepancy between thermodynamically predicted wavespeeds for a reasonable T_{pot} and those required to match MTZ travel times because water leads to

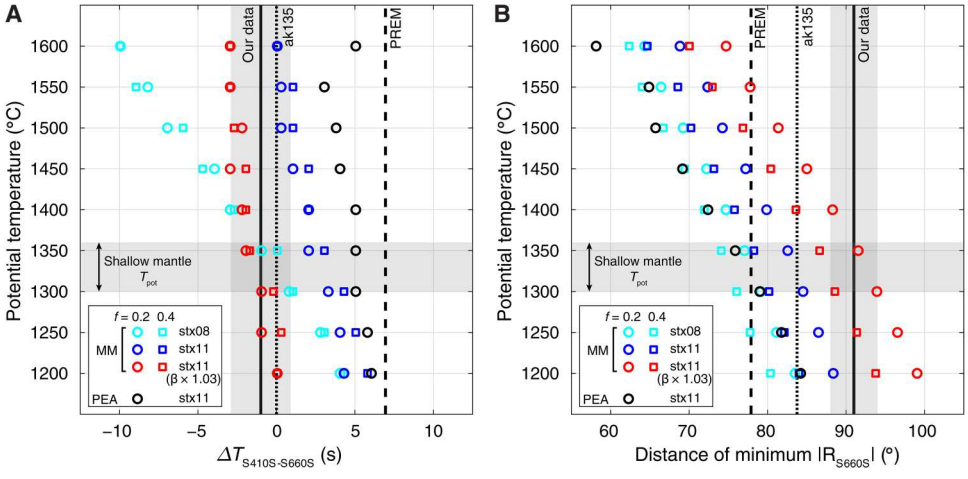

Fig. 6. Constraints on average mantle transition zone (MTZ) temperature. (**A**) Comparison of thermodynamic predictions of differential travel times across the MTZ, $\Delta T_{S410S\text{-}S660S}$, for a range of potential temperatures and compositions, with the seismically measured times from our study and those predicted by global reference models Preliminary Reference Earth Model (PREM) and ak135. $\Delta T_{S410S\text{-}S660S}$ is measured at a distance of 130° on synthetic waveforms calculated by the reflectivity method (*74*). Different thermodynamic databases (stx11 and stx08) predict quite different absolute wavespeeds and $\Delta T_{S410S\text{-}S660S}$, reflecting the uncertainties in the underlying data. As a result, $\Delta T_{S410S\text{-}S660S}$ alone cannot be used to constrain MTZ temperature. (**B**) Distance of the minimum in $|R_{S660S}|$ calculated from thermodynamic models for a range of potential temperatures and compositions. Increasing absolute *S*-wavespeeds by ~3% for mechanical mixture (MM) models from stx11 can reconcile both our observed MTZ differential travel time (~−1 s relative to ak135) and the distance of the minimum in $|R_{S660S}|$ (~91°; Fig. 3C) with shallow mantle temperatures [T_{pot} = 1300° to 1360°C; (*61*)].

slower and likely thicker MTZ (*58*, *59*). Hence, significant global MTZ hydration is difficult to reconcile with the constraints on absolute wavespeed.

Basalt fraction at 410 and 660

The uncertainties in thermodynamic predictions of changes in wavespeed (with phase, temperature, or pressure) are smaller than predictions of absolute wavespeeds, as the former are more strongly constrained by underlying (experimental) data (*19*, *55*). Therefore, we adjust the absolute wavespeeds inferred from the thermodynamically modeled profiles as described above and consider how the predictions of contrasts across 410 and 660 compare with the seismically constrained contrasts (Fig. 4) and the AVO curves (Fig. 3).

It has long been noted that wavespeed contrasts across 410 in global seismic reference models are lower than those expected for a pyrolitic mantle (*35*, *55*, *60*). Although the estimates of wavespeed contrasts from SF1999, LS2006, and our study of 410 reflected and converted waves are higher than those in PREM and ak135, they are still below or at the very low end of estimates for PMM or PEA (Fig. 4). At the same time, wavespeed contrasts at 660, especially for *P* waves, inferred from reflected or converted seismic phases were previously found to be lower than those expected for PMM or PEA (*37*, *38*, *41*), and our results confirm this. Given the uncertainties of thermodynamic estimates of wavespeed contrasts (*55*, *58*), it cannot be ruled out that seismically inferred contrasts could be matched with pyrolitic compositions, but a basalt enrichment would make it easier to reconcile thermodynamic predictions and seismic estimates (Fig. 4) (*35*).

AVO curves provide further constraints. The slopes of the AVO trend of SS and PP precursors depend more strongly on composition than on temperature (compare fig. S21 and fig. S22). To constrain the basalt fraction of the mantle from AVO trends, we only consider a mechanically mixed composition, as it is likely that most of the mantle is MM rather than EA. We calculate the RMSE between observed and synthetic reflectivity as a function of basalt fraction (Fig. 7). For 410, we fit both R_{S410S}/R_{SS} and R_{P410P}/R_{PP} as they are both sensitive to basalt fraction. Given the complexity of P660P, we rely on R_{S660S}/R_{SS} more than on R_{P660P}/R_{PP}. Both stx11 and stx08 require a higher basalt fraction (~40%) for the 660 trends than for 410 (Fig. 7). The estimate of basalt fraction at 410 varies between stx11 and stx08, at about 31 and 18%, respectively. The profiles from stx11 and their wavespeed-depth gradients give the better overall fit to the AVO trends of S660S and P660P (compare Fig. 3, C and D and fig. S23, C and D).

Thus, the seismic constraints are most consistent with a basalt-enriched MTZ compared to pyrolite, with stronger enrichment toward the base of the MTZ. The average seismic properties are, however, not exactly representative of the average MTZ temperature and composition because of the nonlinear relation between wavespeeds and temperature and composition [e.g., (*61*)]. Synthetic calculations based on a plate-recycling mantle convection model (*61*) showed that average seismic contrasts are likely an overestimate of the actual contrast expected for average thermal and compositional conditions. If composition is the same at 410 and 660, then this bias is of a similar magnitude at both discontinuities, and, hence, both our estimates of basalt fractions would be systematically low, that is, the MTZ could be more basalt enriched than we estimate. If more basalt accumulates toward 660, then more variance in the wavespeed contrasts is predicted (*61*) and the bias for 660 would be larger than for 410. In this case, the difference in basalt fraction between 410 and 660 would be underestimated in our analysis. So even within these uncertainties, the seismic constraints indicate a higher basalt fraction near 660 than near 410.

A water-bearing MTZ relative to mantle above could aid in explaining the smaller seismically observed contrast at 410 than expected for a PMM or PEA composition (*58*), without the need for a higher basalt content. That is, the basalt fraction at 410 could then be pyrolitic. At 660, however, a hydrous MTZ would increase the wavespeed contrast relative to the shallow lower mantle (*58*), which would increase the discrepancy between the seismic and PMM or PEA contrasts and require even higher basalt fraction (which would also make less ringwoodite available for holding the water). Therefore, the presence of water would require more basalt enrichment at 660 compared to at 410. We conclude that despite considerable uncertainties in seismic constraints and mineral physics-based forward models, evidence points toward basalt enrichment in the MTZ, especially toward its base.

Dynamic implications

Basalt accumulation in the MTZ has long been proposed (*7*, *60*), but direct observational evidence has remained elusive. Basalt accumulation at the base of MTZ, or the complementary harzburgite enrichment directly below it, has been reported in some regional studies, such as in southern Africa (*62*), northern China (*63*), the Samoa hot spot (*64*), the Hawaii hot spot (*45*), and a few subduction zones (*65*). Our results provide direct seismic evidence for basalt enrichment in the MTZ on a global scale, where it should be borne in mind that the lateral distribution of basalt-rich material may be highly heterogeneous. Further studies are needed to map the spatial distribution of compositional heterogeneity, which may help to understand better the history and the planform of mantle convection.

Basalt accumulation in the MTZ can result from compositional segregation of basaltic crust from harzburgitic mantle lithosphere either along low-viscosity layers that allow delamination in subducting plates or, more likely, in hot, low-viscosity regions in the deep mantle and subsequent entrainment in upwellings (*18*, *20*, *25*, *66*–*68*). Because of the density crossover of basalt relative to harzburgite near 660, segregated basalt tends to be gravitationally trapped near the base of MTZ (Fig. 8). Recent global thermochemical simulations predicted a basalt-enriched reservoir in the MTZ for a wide range of mantle viscosity profiles (*18*). The estimates of the basalt fraction in the MTZ ranges from ~30 to 50% and peaks near 660, with the strength of the compositional gradient across the MTZ depending on the viscosity profile. Our estimates of basalt fractions agree best with the convection models where the MTZ has a higher viscosity than the mantle above.

Basalt enrichment in the MTZ, laterally variable or not, can reconcile the longstanding discordance between geophysical and geochemical perspectives, where the former suggests deep mantle circulation [e.g., (*69*)], while the latter requires preservation of isolated geochemical reservoirs (often equated with the entire lower mantle). Geochemical data require that there are parts of the mantle where basaltic oceanic crust accumulates, hence depleting other parts of the mantle in these components (*70*). In plate recycling models, basalt concentrates deep in the MTZ and in the lowermost mantle, and thereby the lower mantle becomes, on average, enriched in silica relative to a (pyrolitic) uppermost mantle that is

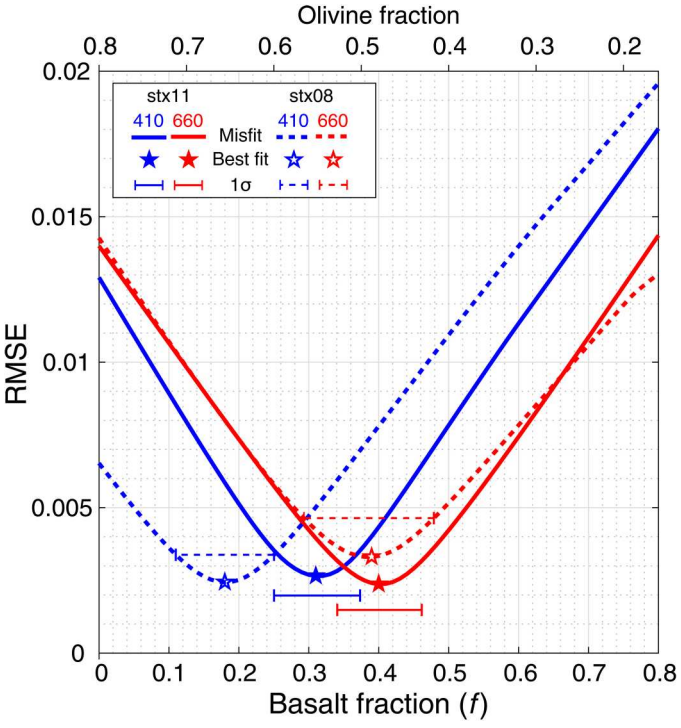

Fig. 7. Constraints on average mantle transition zone (MTZ) composition. Estimate of basalt (and olivine) fraction at 410 and 660. Blue and red curves show root mean square error (RMSE) of reflectivity at 410 and 660, respectively (Fig. 3 and fig. S23). Solid and dashed curves are for stx11 and stx08 databases, respectively.

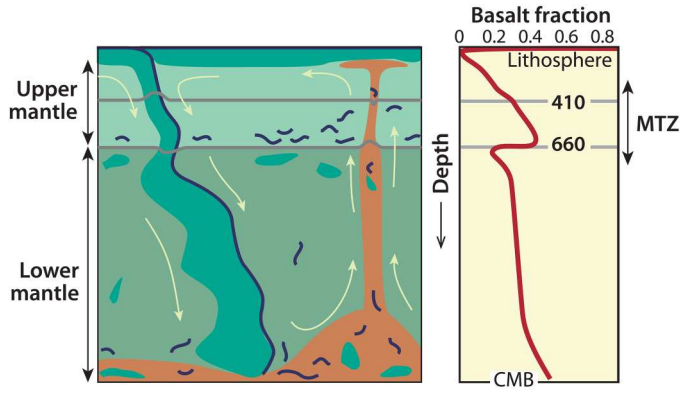

Fig. 8. Interpretation of basalt accumulation in the mantle. The left panel shows a cartoon [modified after (*61*)] of possible mechanisms for basalt segregation during plate recycling, which mainly occurs in hot, low-viscosity regions in the deeper mantle and results in basalt accumulation in the lowermost mantle and the mantle transition zone (MTZ). The right panel shows a sketch of basalt fraction as a function of depth, which is similar to those predicted by the plate recycling model of Yan *et al.* (*18*). Basalt fraction in the lower mantle is expected to be higher than the mid-ocean ridge basalt (MORB) source uppermost mantle, with peaks in the MTZ and just above the core-mantle boundary (CMB).

the source of mid-ocean ridge basalts (MORBs) (*11*, *18*). Silica enrichment of the lower mantle, possibly with substantial lateral heterogeneity, can also help explain average lower mantle radial seismic wavespeed profiles (*71*, *72*). These observations indicate that the overall mantle may well be more silica rich than the often-assumed pyrolitic composition and, thus, that the bulk Earth composition is be more similar to that of CI chondrites. However, in contrast to canonical layered convection models, this average enrichment is not achieved by wholesale (static) differences between the upper and lower mantle but is a direct consequence of large-scale mantle flow combined with basalt segregation near the base of the MTZ and in the deepest regions of the mantle.

MATERIALS AND METHODS

Data preprocessing

We collected all available long-period (1-Hz sampling rate) seismic waveform data for $M \geq 6.0$ earthquakes between 2000 and 2017 from the Data Management Center of Incorporated Research Institutions for Seismology (IRIS), the European Integrated Data Archive of Observatories and Research Facilities for European Seismology (ORFEUS), and between 2013 and 2016 from the China Earthquake Networks Center. Our seismic data preprocessing is similar to previous studies (*44*). We first rotate seismograms from vertical-north-east components into vertical-radial-transverse components based on locations of events and stations. All seismograms are then bandpass-filtered with a two-pass Butterworth filter with corner frequencies at 0.02 and 0.05 Hz. The vertical and transverse components are used for PP and SS precursor studies, respectively. To handle millions of seismograms, we develop an automatic algorithm that can efficiently select and align seismograms. For each event, we discard seismograms with low signal-to-noise ratios [defined as the ratio between maximum amplitude in the main PP and SS window and that in their precursor window (*44*)], low cross-correlation coefficients with other seismograms, and scattered reference phases. Seismograms are then aligned along their peaks based on time shifts obtained from maximizing cross-correlation coefficients. Polarities are corrected if necessary. Last, we visually inspect seismograms to ensure the reliability of our automatic data processing scheme. We process both shallow- (<70 km) and deep- (>70 km) focus earthquakes. Figure 1 (B to D) shows the global distribution of earthquakes and stations and the density of SS and PP bounce points.

SS and PP stacks

We group global SS and PP waveforms according to their bounce points into 768 evenly distributed caps. Cap centers are generated on the basis of the Hierarchical Equal Area isoLatitude Pixelization software (*73*). The radius of each cap is 10° (Fig. 1, C and D), which is close to the size of the first Fresnel zone of SS and PP precursors and also balance the trade-off between data volume in each stack and lateral smoothing. In each cap, we linearly stack SS and PP waveforms as a function of epicentral distances at a grid of 0.5°. To account for the difference in focal depth, a correction term is applied to the epicentral distance by extrapolating SS and PP rays backward from the source to the free surface. The correction term is negligible for shallow-focus events but becomes important for deep-focus events. Amplitudes of SS and PP phases are normalized to unity before stacking. We stack seismograms in the distance range from 60° to 180° but only use data between 70° and 170° for further analysis to minimize edge effects and to avoid large Fresnel zones at large offsets. The results are then averaged over all caps to derive a global stack. Our global stack is more

representative of the true global averaged result as it is equally weighted for all caps and thus is less biased by the uneven distribution of SS and PP bounce points.

SS and PP precursor wavefield separation

The original SS and PP stacks are contaminated by interfering phases and random noise. For example, SS precursors are contaminated by multiples of S/ScS/Sdiff and precursors of ScSScS. PP precursors are strongly contaminated by multiples of P/PcP/Pdiff, PKP branches and their multiples, and precursors of PcPPcP. Conventionally, only limited data within the relatively clean distance window are used for SS and PP precursor studies [e.g., (*38*)]. Here, we apply a curvelet-based array denoising algorithm to remove interfering phases and random noise. The denoising algorithm was developed and tested by Yu *et al.* (*44*). To minimize signal-generated noise and edge effects, we further improve the algorithm using a wild amplitude attenuation algorithm before denoising, which is commonly used in exploration seismology. This algorithm first calculates the median value of absolute amplitudes over all distances at each time step. It then attenuates the amplitudes of interfering phases or wild points to a certain threshold, which is typically several times the median value. We verified our improved denoising algorithm using synthetic waveform modeling (figs. S1 and S2). We apply the improved denoising algorithm to SS and PP stacks for all caps, which are then averaged to derive a global denoised stack. The precursor signals are well separated from interfering phases and random noise (fig. S3). Results of global SS and PP stacks are robust for various data selection criteria (figs. S4 and S5). We also successfully retrieve SS and PP precursors by stacking deep-focus (>70 km) earthquakes, which conventionally were discarded to avoid interference from depth phases (fig. S10).

Amplitudes and reflection coefficients of SS and PP precursors

We measure amplitude ratios of SS and PP precursors relative to their reference phases (i.e., A_{S410S}/A_{SS}, A_{S660S}/A_{SS}, A_{P410P}/A_{PP}, and A_{P660P}/A_{PP}) using a time window of [−30 30] s around their theoretical arrivals. Amplitude ratios of SS and PP precursors are affected by reflection coefficients at discontinuity depths and the free surface, geometrical spreading, intrinsic attenuation, and incoherent stacking. We follow the methodology as in Yu *et al.* (*45*) to recover reflection coefficient ratios of SS and PP precursors with respect to their reference phases (i.e., R_{S410S}/R_{SS}, R_{S660S}/R_{SS}, R_{P410P}/R_{PP}, and R_{P660P}/R_{PP}) by removing effects of geometrical spreading and intrinsic attenuation using parameters from the 1D PREM reference model (Eqs. 1 and 2). Geometrical spreading and intrinsic attenuation corrections using other reference models yield similar results.

$$\frac{R_{SdS}}{R_{SS}} = \frac{A_{SdS}}{A_{SS}} \cdot \left(\frac{G_{SdS}}{G_{SS}} \cdot \frac{Q_{SdS}}{Q_{SS}}\right)^{-1} \quad (1)$$

$$\frac{R_{PdP}}{R_{PP}} = \frac{A_{PdP}}{A_{PP}} \cdot \left(\frac{G_{PdP}}{G_{PP}} \cdot \frac{Q_{PdP}}{Q_{PP}}\right)^{-1} \quad (2)$$

where R is the reflection coefficient, A is the amplitude, G is the geometrical spreading, and Q is the seismic quality factor.

Incoherent stacking of SS and PP precursors is also corrected for the global stack. For each cap, we measure an averaged δT_{SS-SdS} and δT_{PP-PdP} (deviations from 1D reference model) on the denoised stack using data between 110° and 160°, which are usually clean and not strongly affected by phase shifts. Observed arrival times of SS and PP precursors are measured by picking the maximum peaks within a time window of [−30 30] s around their theoretical predictions. Figure S6 shows the global lateral variations in $\delta T_{SS-S410S}$, $\delta T_{SS-S660S}$, and $\delta T_{S410S-S660S}$. The SDs of $\delta T_{SS-S410S}$, $\delta T_{SS-S660S}$, and $\delta T_{S410S-S660S}$ are 2.5, 2.7, and 1.9 s, respectively. Figure S7 shows the global lateral variations in $\delta T_{PP-P410P}$. The SDs of $\delta T_{PP-P410P}$ is 1.4 s. The ratio of SD between $\delta T_{SS-S410S}$ and $\delta T_{PP-P410P}$ is about 1.86, in good agreement with the bulk V_P/V_S ratio of the upper mantle of the PREM reference model, demonstrating the reliability of our estimations. P660P, however, is too weak to be readily picked. We assume that the ratio of SD between $\delta T_{SS-S660S}$ and $\delta T_{PP-P660P}$ is the same as that between $\delta T_{SS-S410S}$ and $\delta T_{PP-P410P}$. Using the stacked SS and PP wavelets as inputs, we estimate the amplitude reductions of S410S, S660S, P410P, and P660P due to incoherent stacking. Figure S8 shows amplitude correction terms of geometrical spreading, intrinsic attenuation, and incoherent stacking for S410S, S660S, P410P, and P660P. The resulting reflection coefficient ratios of shallow and shallow-focus (<70 km) and deep-focus (>70 km) earthquakes are shown in figs. S9 and S11, respectively.

Synthetic waveform modeling

We calculate the synthetic waveforms in two different ways. First, we use the reflectivity method (*74*) to calculate full synthetic waveforms, which include both desired phases and interfering phases (fig. S1, A and D). Second, we use the propagator matrix algorithm (*50*) to compute the full reflectivity of SS and PP precursors. The propagator matrix algorithm is computationally efficient. It is also free from contamination by interfering phases, which makes it well suited to analyze the amplitude and arrival time properties of SS and PP and their precursors. The source wavelet is assumed to be a Ricker function, whose width is adjusted to match globally stacked SS and PP source wavelets. The algorithm is benchmarked using a simple model contains 410 and 660 discontinuities only, for which the calculated reflectivity of SS and PP precursors perfectly matches theoretical predictions using Zoeppritz equations. We note that the propagator matrix algorithm uses flat-layered Earth models and assumes plane wave incidence. So, the reflectivity at 410 and 660 needs to be calculated separately in the propagator matrix algorithm to compare with those calculated by the reflectivity method (*74*), which uses spherical Earth models. The reflectivity at 410 and 660 calculated by these two methods are consistent (fig. S2). The absolute arrival times of SS and PP precursors are only slightly different (fig. S1).

SS and PP reflection coefficients near the free surface

To recover elastic properties across 410 and 660, we also need to calculate reflection coefficients near the free surface. SS reflection coefficients (R_{SS}) at the free surface simply equal to 1 for all distances. However, because of the interference from other reflections from lithospheric discontinuities, especially the Moho, the effective reflection coefficients could be different. We estimate the effect of crustal thickness on effective R_{SS} using synthetic waveform modeling. In general, the effective R_{SS} is only slightly different from 1. The

maximum perturbation is about ±5% (fig. S12). For the PP phase, R_{PP} increases as a function of epicentral distance. The existence of a Moho discontinuity generally results in a decrease or increase in the effective R_{PP} when the Moho is shallow or relatively deep, respectively. The maximum perturbation is about ±15% (fig. S12). In addition, the existence of a thick water column can change the effective R_{PP} (*50*). It is not easy to accurately quantify this effect as it is model and frequency dependent. Here, for simplicity, we assume that phase interference from lithospheric discontinuities cancels out or does not affect the free surface reflections for the global stack. We use a half-space crustal layer (with *P*-wavespeed, *S*-wavespeed, and density equal to 6.3 km/s, 3.5 km/s, and 2.8×10^3 kg/m^3, respectively) to calculate R_{SS} and R_{PP}. We expect that uncertainties due to the free surface reflection coefficients in globally averaged R_{SS} and R_{PP} are insignificant.

Effect of elastic structure on the amplitude and apparent moveout of S660S and P660P

First, we test the effect of $\Delta\rho_{660}/\Delta\beta_{660}$ on the amplitude and apparent moveout of S660S. We use simplified thermodynamic models, in which wavespeed and density gradients above and below 660 are set to constants. The width of 660 is set to 5 km. Mean β_{660} is set to be the same as that of ak135. Smaller and larger $\Delta\rho_{660}/\Delta\beta_{660}$ tend to shift the reflectivity and moveout curve to larger and smaller epicentral distance, respectively (figs. S14 and S15). Absolute values of $\Delta\beta_{660}$ (or $\Delta\rho_{660}$) with the same $\Delta\rho_{660}/\Delta\beta_{660}$ ratio only modulate the amplitudes, without changing the moveout curve. Fitting observed arrival times of S660S gives a $\Delta\rho_{660}/\Delta\beta_{660}$ close to that (~0.87) of thermodynamic models, which is consistent with the estimation from the observed distance of the minimum in $|R_{S660S}|$ (fig. S13).

Next, we test the effect of $\Delta\alpha_{660}/\Delta\beta_{660}$ on the amplitude and apparent moveout of P660P. $\Delta\beta_{660}$ and $\Delta\rho_{660}$ are fixed using the above estimates. We find that the amplitude and apparent moveout of P660P strongly depends on $\Delta\alpha_{660}/\Delta\beta_{660}$ (figs. S16 and S17). As $\Delta\alpha_{660}/\Delta\beta_{660}$ increases, the transitional region of the moveout curve shifts toward smaller epicentral distance and the magnitude of moveout diminishes. At the same time, amplitudes of P660P increase at larger epicentral distances but first decrease and then increase at smaller epicentral distances. Fitting the observed moveout curve of P660P require a $\Delta\alpha_{660}/\Delta\beta_{660}$ of about 0.54, which is tightly constrained.

Last, we test the effect of wavespeed and density gradients around 660 on the amplitude and apparent moveout of S660S and P660P. Because P660P reflectivity is small, the observed amplitude is no longer sensitive to 660 itself but sensitive to the wavespeed and density gradients around it. We find that the observed moveout of P660P is most sensitive to wavespeed and density gradients below 660. Figure S18 shows synthetic reflectivity and apparent moveout of S660S and P660P for various wavespeed and density gradients below 660. The wavespeed and density gradients above 660 are fixed to be similar to those of the thermodynamic models. Lower gradients below 660 result in an opposite apparent moveout trend of P660P, and higher gradients below 660 result in large P660P amplitude at small epicentral distances (figs. S18 and S19). Amplitude and apparent moveout of S660S are generally insensitive to wavespeed and density gradients around 660 (fig. S18).

Thermodynamic modeling

We assume that the mantle composition is a mechanical mixture of basalt and harzburgite with basalt fraction ranging from 0 to 80%. We also consider the cases of an equilibrium assemblage and mechanical mixture of bulk pyrolitic composition. A basalt fraction of ~18% in a mechanical mixture yields a bulk mantle composition identical to pyrolite (*34*). This value would be smaller if mantle melting leaves behind a more fertile residue than harzburgite. Most studies find that the basalt fraction in the mantle that forms the source of MORBs is less than 20% (*34*, *75*, *76*). The adiabatic mantle potential temperature is varied from 1200° to 1600°C at an increment of 50°C spanning a range of plausible mantle temperatures. The corresponding seismic wavespeed and density profiles are thermodynamically modeled following the methods described by Cobden *et al.* (*77*). The code PerPle_X (*78*) is used to perform Gibbs free-energy minimization and compute bulk moduli, shear moduli, and density using the equations of state from Stixrude and Lithgow-Bertelloni (*79*), with either the internally self-consistent thermodynamic parameters and solid solution models from Stixrude and Lithgow-Bertelloni (*19*) (stx11) or those from Xu *et al.* (*34*) (stx08). We apply an anelasticity correction using the temperature-, pressure-, and frequency-dependent model Q7, which yields a *Q*-depth structure in agreement with seismic average global *Q* models and seismically imaged lateral *Q* variations [parameters described in (*64*), following Matas and Bukowinski (*80*)]. We tested that the choice of anelasticity model has little effect on the results at the MTZ temperature and pressure conditions considered.

Estimating uncertainties for the thermodynamic modeling is challenging, because parameters are constrained by a wide range of experimental and numerical studies and/or systematics from related phases, and several of the parameters are correlated, often in complex ways. SDs for the individual parameters in the databases (*19*, *34*) translate into considerable uncertainties in both absolute wavespeeds and wavespeed contrasts across discontinuities predicted by the thermodynamic models (*55*, *58*, *81*). Uncertainties in absolute values are larger than in differences between wavespeeds as a function of phase, temperature, or pressure (*81*). Furthermore, some of the thermodynamic parameters are strongly correlated (e.g., only certain combinations of zero pressure moduli and pressure derivatives will match underlying experimental data, and only particular combinations of olivine and wadleyite parameters will be compatible with experimental constraints on phase boundaries as a function of temperature and pressure). In a number of ways, the stx11 database is an improvement over stx08, as it incorporates more and newer data and includes an additional oxide, sodium, thus allowing a more complete description of mantle composition, particularly of basaltic components. Some additional phases that play a role in the shallowest and deepest mantle were added in the stx11 database. In other respects, differences in predictions from the two databases are not directly constrained by underlying data and represent alternative outcomes possible within the uncertainties of the data. Some differences reflect continuing debates over mantle parameters, e.g., the effective Clapeyron slope for the ringwoodite to postspinel transition in stx11 is on the low end of the range in published experimental and seismic studies (*23*, *61*). Common outcomes from the two databases are more likely to correspond to robust features.

Supplementary Materials

This PDF file includes:

Figs. S1 to S23
Table S1

REFERENCES AND NOTES

1. A. Ringwood, A model for the upper mantle. *J. Geophys. Res.* **67**, 857–867 (1962).
2. W. F. McDonough, S.-S. Sun, The composition of the Earth. *Chem. Geol.* **120**, 223–253 (1995).
3. H. Palme, H. S. C. O'Neill, Cosmochemical estimates of mantle composition. *Treatise Geochemistry* **2**, 568 (2003).
4. T. Lyubetskaya, J. Korenaga, Chemical composition of Earth's primitive mantle and its variance: 1. Method and results. *J. Geophys. Res. Solid Earth* **112**, B03211 (2007).
5. S. R. Hart, A. Zindler, In search of a bulk-Earth composition. *Chem. Geol.* **57**, 247–267 (1986).
6. J. Ita, L. Stixrude, Petrology, elasticity, and composition of the mantle transition zone. *J. Geophys. Res. Solid Earth* **97**, 6849–6866 (1992).
7. D. L. Anderson, J. D. Bass, Transition region of the Earth's upper mantle. *Nature* **320**, 321–328 (1986).
8. T. Irifune, Phase transformations in the earth's mantle and subducting slabs: Implications for their compositions, seismic velocity and density structures and dynamics. *Island Arc* **2**, 55–71 (1993).
9. G. R. Helffrich, B. J. Wood, The Earth's mantle. *Nature* **412**, 501–507 (2001).
10. P. E. van Keken, E. H. Hauri, C. J. Ballentine, Mantle mixing: The generation, preservation, and destruction of chemical heterogeneity. *Annu. Rev. Earth Planet. Sci.* **30**, 493–525 (2002).
11. M. D. Ballmer, N. C. Schmerr, T. Nakagawa, J. Ritsema, Compositional mantle layering revealed by slab stagnation at ~1000-km depth. *Sci. Adv.* **1**, e1500815 (2015).
12. C. J. Allègre, D. L. Turcotte, Implications of a two-component marble-cake mantle. *Nature* **323**, 123–127 (1986).
13. L. Stixrude, C. Lithgow-Bertelloni, Geophysics of chemical heterogeneity in the mantle. *Annu. Rev. Earth Planet. Sci.* **40**, 569–595 (2012).
14. A. W. Hofmann, S. R. Hart, An assessment of local and regional isotopic equilibrium in the mantle. *Earth Planet. Sci. Lett.* **38**, 44–62 (1978).
15. A. Zindler, S. Hart, Chemical geodynamics. *Annu. Rev. Earth Planet. Sci.* **14**, 493–571 (1986).
16. T. D. Jones, N. Sime, P. E. van Keken, Burying earth's primitive mantle in the slab graveyard. *Geochem. Geophys. Geosyst.* **22**, e2020GC009396 (2021).
17. T. Nakagawa, P. J. Tackley, F. Deschamps, J. A. Connolly, The influence of MORB and harzburgite composition on thermo-chemical mantle convection in a 3-D spherical shell with self-consistently calculated mineral physics. *Earth Planet. Sci. Lett.* **296**, 403–412 (2010).
18. J. Yan, M. D. Ballmer, P. J. Tackley, The evolution and distribution of recycled oceanic crust in the Earth's mantle: Insight from geodynamic models. *Earth Planet. Sci. Lett.* **537**, 116171 (2020).
19. L. Stixrude, C. Lithgow-Bertelloni, Thermodynamics of mantle minerals - II. Phase equilibria. *Geophys. J. Int.* **184**, 1180–1213 (2011).
20. A. E. Ringwood, Phase transformations and their bearing on the constitution and dynamics of the mantle. *Geochim. Cosmochim. Acta* **55**, 2083–2110 (1991).
21. D. J. Weidner, Y. Wang, Phase transformations: Implications for mantle structure. *Geophys. Monogr. Am. Geophys. Union* **117**, 215–235 (2000).
22. U. Christensen, Effects of phase transitions on mantle convection. *Annu. Rev. Earth Planet. Sci.* **23**, 65–87 (1995).
23. M. Faccenda, L. Dal Zilio, The role of solid–Solid phase transitions in mantle convection. *Lithos* **268-271**, 198–224 (2017).
24. S. Goes, R. Agrusta, J. van Hunen, F. Garel, Subduction-transition zone interaction: A review. *Geosphere* **13**, 644–664 (2017).
25. J. Van Summeren, A. Van den Berg, R. Van der Hilst, Upwellings from a deep mantle reservoir filtered at the 660km phase transition in thermo-chemical convection models and implications for intra-plate volcanism. *Phys. Earth Planet. Inter.* **172**, 210–224 (2009).
26. P. M. Shearer, T. G. Masters, Global mapping of topography on the 660-km discontinuity. *Nature* **355**, 791–796 (1992).
27. M. P. Flanagan, P. M. Shearer, Global mapping of topography on transition zone velocity discontinuities by stacking SS precursors. *J. Geophys. Res. Solid Earth* **103**, 2673–2692 (1998).
28. Y. J. Gu, A. M. Dziewonski, Global variability of transition zone thickness. *J. Geophys. Res. Solid Earth* **107**, 2135 (2002).
29. S. Lebedev, S. Chevrot, R. D. van der Hilst, Seismic evidence for olivine phase changes at the 410- and 660-kilometer discontinuities. *Science* **296**, 1300–1302 (2002).
30. C. Houser, G. Masters, M. Flanagan, P. Shearer, Determination and analysis of long-wavelength transition zone structure using SS precursors. *Geophys. J. Int.* **174**, 178–194 (2008).
31. J. F. Lawrence, P. M. Shearer, Imaging mantle transition zone thickness with SdS-SS finite-frequency sensitivity kernels. *Geophys. J. Int.* **174**, 143–158 (2008).
32. A. Deuss, Global observations of mantle discontinuities using SS and PP precursors. *Surv. Geophys.* **30**, 301–326 (2009).
33. L. Waszek, B. Tauzin, N. C. Schmerr, M. D. Ballmer, J. C. Afonso, A poorly mixed mantle transition zone and its thermal state inferred from seismic waves. *Nat. Geosci.* **14**, 949–955 (2021).
34. W. Xu, C. Lithgow-Bertelloni, L. Stixrude, J. Ritsema, The effect of bulk composition and temperature on mantle seismic structure. *Earth Planet. Sci. Lett.* **275**, 70–79 (2008).
35. T. S. Duffy, D. L. Anderson, Seismic velocities in mantle minerals and the mineralogy of the upper mantle. *J. Geophys. Res. Solid Earth* **94**, 1895–1912 (1989).
36. P. Vacher, A. Mocquet, C. Sotin, Computation of seismic profiles from mineral physics: The importance of the non-olivine components for explaining the 660 km depth discontinuity. *Phys. Earth Planet. Inter.* **106**, 275–298 (1998).
37. C. H. Estabrook, R. Kind, The nature of the 660-kilometer upper-mantle seismic discontinuity from precursors to the PP phase. *Science* **274**, 1179–1182 (1996).
38. P. M. Shearer, M. P. Flanagan, Seismic velocity and density jumps across the 410- and 660-kilometer discontinuities. *Science* **285**, 1545–1548 (1999).
39. K. Chambers, A. Deuss, J. Woodhouse, Reflectivity of the 410-km discontinuity from PP and SS precursors. *J. Geophys. Res. Solid Earth* **110**, B02301 (2005).
40. A. Deuss, S. A. Redfern, K. Chambers, J. H. Woodhouse, The nature of the 660-kilometer discontinuity in Earth's mantle from global seismic observations of PP precursors. *Science* **311**, 198–201 (2006).
41. J. F. Lawrence, P. M. Shearer, Constraining seismic velocity and density for the mantle transition zone with reflected and transmitted waveforms. *Geochem. Geophys. Geosyst.* **7**, 10012 (2006).
42. S. Lessing, C. Thomas, M. Saki, N. Schmerr, E. Vanacore, On the difficulties of detecting PP precursors. *Geophys. J. Int.* **201**, 1666–1681 (2015).
43. B. Tauzin, L. Waszek, M. D. Ballmer, J. C. Afonso, T. Bodin, Basaltic reservoirs in the Earth's mantle transition zone. *Proc. Natl. Acad. Sci. U.S.A.* **119**, e2209399119 (2022).
44. C. Yu, E. A. Day, M. V. de Hoop, M. Campillo, R. D. van der Hilst, Mapping mantle transition zone discontinuities beneath the Central Pacific with array processing of SS precursors. *J. Geophys. Res. Solid Earth.* **122**, 10,364–10,378 (2017).
45. C. Yu, E. A. Day, M. V. de Hoop, M. Campillo, S. Goes, R. A. Blythe, R. D. van der Hilst, Compositional heterogeneity near the base of the mantle transition zone beneath Hawaii. *Nat. Commun.* **9**, 1266 (2018).
46. A. M. Dziewonski, D. L. Anderson, Preliminary reference Earth model. *Phys. Earth Planet. Inter.* **25**, 297–356 (1981).
47. B. Kennett, E. Engdahl, R. Buland, Constraints on seismic velocities in the Earth from traveltimes. *Geophys. J. Int.* **122**, 108–124 (1995).
48. J.-P. Montagner, B. Kennett, How to reconcile body-wave and normal-mode reference Earth models. *Geophys. J. Int.* **125**, 229–248 (1996).
49. K. Aki, P. G. Richards, *Quantitative seismology* (University Science Books, Sausalito, Calif, 2002), vol. 1.
50. Y. Zhou, X. Chen, D. Yuen, M. Xu, Effects of near-surface complexities on differential travel times and amplitude ratios between PP and its precursors. *J. Geophys. Res. Solid Earth* **125**, e2019JB019139 (2020).
51. J. Ritsema, W. Xu, L. Stixrude, C. Lithgow-Bertelloni, Estimates of the transition zone temperature in a mechanically mixed upper mantle. *Earth Planet. Sci. Lett.* **277**, 244–252 (2009).
52. C. Herzberg, P. D. Asimow, N. Arndt, Y. Niu, C. M. Lesher, J. G. Fitton, M. J. Cheadle, A. D. Saunders, Temperatures in ambient mantle and plumes: Constraints from basalts, picrites, and komatiites. *Geochem. Geophys. Geosyst.* **8**, Q02006 (2007).
53. C. A. Dalton, C. H. Langmuir, A. Gale, Geophysical and geochemical evidence for deep temperature variations beneath mid-ocean ridges. *Science* **344**, 80–83 (2014).
54. F. Richards, M. Hoggard, A. Crosby, S. Ghelichkhan, N. White, Structure and dynamics of the oceanic lithosphere-asthenosphere system. *Phys. Earth Planet. Inter.* **309**, 106559 (2020).
55. F. Cammarano, A. Deuss, S. Goes, D. Giardini, One-dimensional physical reference models for the upper mantle and transition zone: Combining seismic and mineral physics constraints. *J. Geophys. Res. Solid Earth* **110**, B01306 (2005).
56. L. Cobden, S. Goes, F. Cammarano, J. A. Connolly, Thermochemical interpretation of one-dimensional seismic reference models for the upper mantle: Evidence for bias due to heterogeneity. *Geophys. J. Int.* **175**, 627–648 (2008).
57. D. Bercovici, S. Karato, Whole-mantle convection and the transition-zone water filter. *Nature* **425**, 39–44 (2003).

58. V. Thio, L. Cobden, J. Trampert, Seismic signature of a hydrous mantle transition zone. *Phys. Earth Planet. Inter.* **250**, 46–63 (2016).
59. J. M. R. Muir, F. Zhang, J. P. Brodholt, The effect of water on the post-spinel transition and evidence for extreme water contents at the bottom of the transition zone. *Earth Planet. Sci. Lett.* **565**, 116909 (2021).
60. D. L. Anderson, The upper mantle transition region: Eclogite? *Geophys. Res. Lett.* **6**, 433–436 (1979).
61. S. Goes, C. Yu, M. D. Ballmer, J. Yan, R. D. van der Hilst, Compositional heterogeneity in the mantle transition zone. *Nat. Rev. Earth Environ.* **3**, 533–550 (2022).
62. Y. Shen, J. Blum, Seismic evidence for accumulated oceanic crust above the 660-km discontinuity beneath southern Africa. *Geophys. Res. Lett.* **30**, 1925 (2003).
63. J. Feng, H. Yao, Y. Wang, P. Poli, Z. Mao, Segregated oceanic crust trapped at the bottom mantle transition zone revealed from ambient noise interferometry. *Nat. Commun.* **12**, 1–8 (2021).
64. R. Maguire, J. Ritsema, S. Goes, Signals of 660 km topography and harzburgite enrichment in seismic images of whole-mantle upwellings. *Geophys. Res. Lett.* **44**, 3600–3607 (2017).
65. F. Bissig, A. Khan, D. Giardini, Evidence for basalt enrichment in the mantle transition zone from inversion of triplicated P- and S-waveforms. *Earth Planet. Sci. Lett.* **580**, 117387 (2022).
66. A. Mambole, L. Fleitout, Petrological layering induced by an endothermic phase transition in the Earth's mantle. *Geophys. Res. Lett.* **29**, 1-1–1-4 (2002).
67. P. J. Tackley, S. Xie, The thermochemical structure and evolution of Earth's mantle: Constraints and numerical models. *Philos. Trans. Royal Soc. London A* **360**, 2593–2609 (2002).
68. C. Lee, W. Chen, Possible density segregation of subducted oceanic lithosphere along a weak serpentinite layer and implications for compositional stratification of the Earth's mantle. *Earth Planet. Sci. Lett.* **255**, 357–366 (2007).
69. R. Van der Hilst, S. Widiyantoro, E. Engdahl, Evidence for deep mantle circulation from global tomography. *Nature* **386**, 578–584 (1997).
70. J. M. Tucker, P. E. van Keken, R. E. Jones, C. J. Ballentine, A role for subducted oceanic crust in generating the depleted mid-ocean ridge basalt mantle. *Geochem. Geophys. Geosyst.* **21**, e2020GC009148 (2020).
71. F. Deschamps, J. Trampert, Towards a lower mantle reference temperature and composition. *Earth Planet. Sci. Lett.* **222**, 161–175 (2004).
72. J. Matas, J. Bass, Y. Ricard, E. Mattern, M. S. T. Bukowinski, On the bulk composition of the lower mantle: Predictions and limitations from generalized inversion of radial seismic profiles. *Geophys. J. Int.* **170**, 764–780 (2007).
73. K. M. Górski, E. Hivon, A. J. Banday, B. D. Wandelt, F. K. Hansen, M. Reinecke, M. Bartelmann, HEALPix: A framework for high-resolution discretization and fast analysis of data distributed on the sphere. *Astrophys. J.* **622**, 759–771 (2005).
74. K. Fuchs, G. Müller, Computation of synthetic seismograms with the reflectivity method and comparison with observations. *Geophys. J. Int.* **23**, 417–433 (1971).
75. P. J. Morgan, W. J. Morgan, Two-stage melting and the geochemical evolution of the mantle: A recipe for mantle plum-pudding. *Earth Planet. Sci. Lett.* **170**, 215–239 (1999).
76. A. V. Sobolev, A. W. Hofmann, D. V. Kuzmin, G. M. Yaxley, N. T. Arndt, S.-L. Chung, L. V. Danyushevsky, T. Elliott, F. A. Frey, M. O. Garcia, The amount of recycled crust in sources of mantle-derived melts. *Science* **316**, 412–417 (2007).
77. L. Cobden, S. Goes, M. Ravenna, E. Styles, F. Cammarano, K. Gallagher, J. A. Connolly, Thermochemical interpretation of 1-D seismic data for the lower mantle: The significance of nonadiabatic thermal gradients and compositional heterogeneity. *J. Geophys. Res. Solid Earth* **114**, B11309 (2009).
78. J. A. D. Connolly, Computation of phase equilibria by linear programming: A tool for geodynamic modeling and its application to subduction zone decarbonation. *Earth Planet. Sci. Lett.* **236**, 524–541 (2005).
79. L. Stixrude, C. Lithgow-Bertelloni, Thermodynamics of mantle minerals - I. Physical properties. *Geophys. J. Int.* **162**, 610–632 (2005).
80. J. Matas, M. S. T. Bukowinski, On the anelastic contribution to the temperature dependence of lower mantle seismic velocities. *Earth Planet. Sci. Lett.* **259**, 51–65 (2007).
81. F. Cammarano, S. Goes, P. Vacher, D. Giardini, Inferring upper-mantle temperatures from seismic velocities. *Phys. Earth Planet. Inter.* **138**, 197–222 (2003).

Acknowledgments: C.Y. thanks Y. Zhou for sharing the propagator matrix algorithm code and J. Hu for assisting in the denoising algorithm. **Funding:** C.Y. acknowledges funding from NSFC under grant nos. 92155307 and 42174058 and the Guangdong Provincial Key Laboratory of Geophysical High-resolution Imaging Technology (2022B1212010002). **Author contributions:** This study was conceived by all authors. C.Y. conducted seismological analyses. S.G. ran the thermodynamic modeling. C.Y. and S.G. drafted the original manuscript with inputs from all authors. Figures were prepared by C.Y. and S.G. All authors contributed to the discussions and interpretations of results. **Competing interests:** The authors declare that they have no competing interests. **Data and materials availability:** All data needed to evaluate the conclusions in the paper are present in the paper and/or the Supplementary Materials. Original seismic waveform data are obtained from the Data Management Center of IRIS (www.iris.edu), European Integrated Data Archive of ORFEUS (www.orfeus-eu.org), and China Earthquake Networks Center, National Earthquake Data Center (http://data.earthquake.cn). Wavespeed and density profiles from our thermodynamic modeling are available at https://zenodo.org/record/7694783. Codes for calculating SS and PP reflection coefficients at a solid-solid interface or at the free surface are available at https://zenodo.org/record/5989602.

Submitted 26 November 2022
Accepted 21 April 2023
Published 31 May 2023
10.1126/sciadv.adg0095